

On-chip transfer of ultrashort graphene plasmon wavepackets using terahertz electronics

Katsumasa Yoshioka^{1,*}, Guillaume Bernard¹, Taro Wakamura¹, Masayuki Hashisaka¹, Ken-ichi Sasaki¹, Satoshi Sasaki¹, Kenji Watanabe², Takashi Taniguchi³, and Norio Kumada¹

¹NTT Basic Research Laboratories, NTT Corporation,
3-1 Morinosato-Wakamiya, Atsugi, 243-0198, Japan

²Research Center for Electronic and Optical Materials, National Institute for Materials Science,
1-1 Namiki, Tsukuba 305-0044, Japan

³Research Center for Materials Nanoarchitectonics, National Institute for Materials Science,
1-1 Namiki, Tsukuba 305-0044, Japan

*e-mail: katsumasa.yoshioka@ntt.com

Abstract:

Steering transport of ultrashort polariton wavepackets is essential for achieving on-chip integrated nanocircuits with tightly confined electromagnetic fields towards ultrafast information processing. However, conventional optical techniques have struggled to integrate the necessary components for transferring polariton signals. Here, we address this challenge by electrically generating, manipulating, and reading out terahertz graphene plasmon-polariton wavepackets on-chip. By injecting an electrical pulse into graphene via an ohmic contact, we achieve coherent conversion of the pulse into a plasmon wavepacket exhibiting a pulse duration of 1.2 ps and extreme three-dimensional spatial confinement within a volume of $2.1 \times 10^{-18} \text{ m}^3$. We reveal the transport properties of plasmons along graphene ribbons in different dielectric environments, providing a basis for designing graphene plasmonic circuits. Furthermore, we find that the conversion efficiency between the electrical pulses and plasmon wavepackets reaches ~30% thanks to the absence of a momentum mismatch. With unprecedented controllability, our platform represents a significant advance in on-chip handling of plasmonic signals in various van der Waals heterostructures.

Main text:

Graphene plasmon polaritons in the terahertz (THz) and mid-infrared frequency range have attracted significant interest as potential next-generation information carriers due to their strong light confinement capabilities, high controllability through carrier density modulation, and low loss characteristics¹⁻⁵. Various graphene plasmonic circuits have been proposed for both classical⁶⁻⁹ and quantum¹⁰⁻¹² information transfer and processing; these circuits feature active functionalities through electrostatic gating that are unattainable with metallic plasmonic circuits^{13,14}. The fundamental properties of graphene plasmons have been extensively investigated using optical techniques such as far-field spectroscopies¹⁵⁻²³ and near-field scanning optical microscopies²⁴⁻³². However, these methods measure the absorption of localized plasmon resonance¹⁵⁻²³ or standing waves of plasmons²⁴⁻³² and are not directly applicable to operate plasmonic circuits. To fully realize the functionalities of graphene plasmonic circuits, it is crucial to develop a novel methodology capable of efficiently generating dynamically controllable plasmon signals, manipulating their propagation, and remotely measuring their amplitude and phase on-chip. One of the significant obstacles to achieving such a capability is the momentum mismatch between the incident optical excitation and graphene plasmons. While subwavelength structures, such as antennas and gratings, can overcome this mismatch¹⁵⁻³², the conversion efficiency between the optical excitation and the graphene plasmon wavepacket is still low, making the excitation and detection of propagating plasmons challenging. Furthermore, the subwavelength structures restrict the device geometry.

One promising strategy to circumvent the momentum mismatch is injecting spatiotemporally localized electrical pulses, which can transiently create a local charge density imbalance in the system and subsequently launch plasmons. While high-frequency gigahertz (GHz) electronics have indeed been used to make time-resolved transport measurements of graphene plasmons in bulk³³ and quantum Hall edge channels³⁴⁻³⁶, the bandwidth limitations imposed by conventional electronics preclude access to the desired THz range. Consequently, THz electronics and device architectures capable of handling THz plasmons will have to be developed in order to realize graphene plasmonic circuits for fast information transfer and processing.

In this work, we achieved efficient electrical generation, manipulation, and detection of

propagating ultrashort graphene plasmon wavepackets by using on-chip THz spectroscopy³⁷⁻⁴² and integrated circuits consisting of a graphene-embedded coplanar waveguide combined with top-gate structures for controlling the carrier density of graphene. By meticulously engineering the broadband high-frequency circuit response, we enabled dynamic tracking of plasmon wavepackets as short as 1.2 ps on-chip. This is the shortest wavepacket ever created on a material by using high-frequency electronics, and it allowed us to directly investigate crucial metrics such as propagation velocity, spatial confinement, propagation length, and conversion efficiency in graphene micro ribbons in different dielectric environments. These results lay the foundation for realizing a range of graphene plasmonic circuits.

Experimental setup

Our device, illustrated in Fig. 1a, integrates a high-quality single-layer graphene transistor encapsulated with hexagonal boron nitride (hBN) into the center of a coplanar waveguide (CPW). The transmission region of the CPW comprises a 10- μm -wide center conductor flanked by two ground planes, each separated from the center conductor by a 7- μm gap. Both ends of the graphene form ohmic contacts with the center conductor through titanium/gold (Ti/Au) edge contacts⁴³. The graphene was etched into a micro ribbon with a length of over 20 μm and a width of 8 μm . We fabricated two devices with different top-gate structures: one had a ZnO gate and the other had a standard metal (Ti/Au) gate. The ZnO top gate is transparent in the GHz and THz range^{22,41}. This enables us to investigate plasmons free from the gate screening (unscreened plasmons) while tuning the carrier density. In the metal gate device, on the other hand, the screening effect gives rise to acoustic plasmons^{19-21,27,28,31} with the electric field confined between the gate electrode and graphene. Understanding the transport properties of plasmon wavepackets in graphene micro ribbons under different screening conditions is critical for constructing plasmonic circuits with tunable functionalities. Detailed descriptions of these structures are presented in the following sections (Fig. 2 for unscreened and Fig. 3 for acoustic plasmon).

We conducted pump-probe experiments using a pulsed femtosecond laser with a 280-fs pulse duration and a wavelength of 1035 nm to avoid photo-induced doping in graphene⁴¹. The beam was divided into pump and probe beams with a controlled time delay to excite

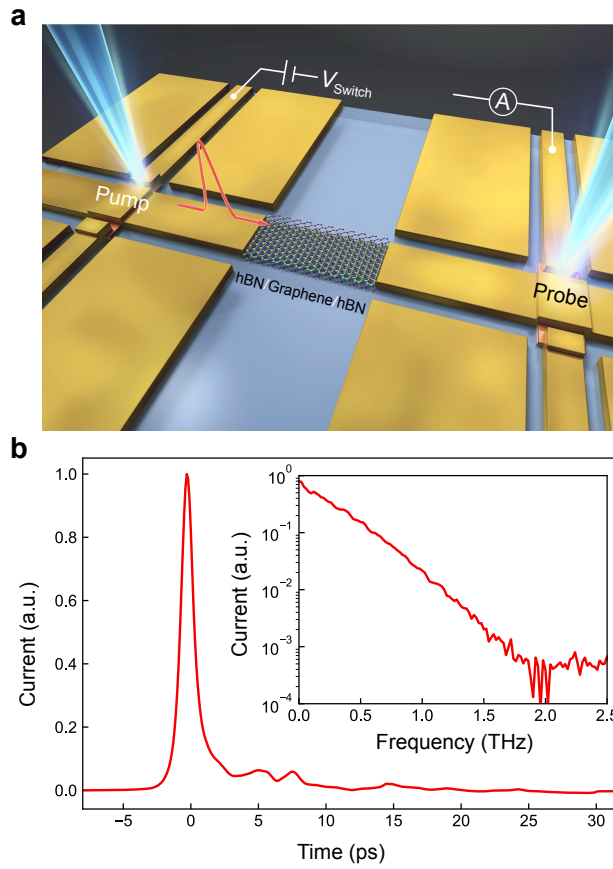


Figure 1 | Terahertz electronics setup. **a**, Schematic device structure. A graphene transistor is integrated into a coplanar waveguide (CPW). Detail gate structures are presented in Figs. 2a, b and Figs. 3a, b. Both ends of the graphene form ohmic contacts with the center conductor of the CPW, facilitating injection and extraction of THz electrical current. The current is generated and measured in the time domain through LT-GaAs PC switches by using a pump-probe method. **b**, Temporal profile of THz electrical current in a CPW without graphene for a travel length of 485 μm . This ultrashort electrical pulse is used to electrically excite graphene plasmons throughout the study. Measurements were performed at 4 K. The inset shows the normalized Fourier-transformed spectrum.

low-temperature-grown gallium arsenide (LT-GaAs) photoconductive (PC) switches placed on either side of the graphene: one PC switch is used to inject a THz electrical pulse into the graphene from one ohmic contact and the other is used to read out the time-domain waveform after it passes through the graphene. Figure 1b shows the waveform of the THz electrical pulse measured using a CPW without graphene. The pulse duration is 1.2 ps at full width at half maximum (FWHM) with the frequency component ranging

from 0 to 2 THz, as shown in the inset. This waveform corresponds to the THz electrical pulse used to electrically excite ultrashort graphene plasmon wavepackets throughout the study. All measurements were performed at 4 K in a vacuum.

Experimental results

Unscreened graphene plasmons in a ZnO gate device

Let us begin by investigating the transport properties of unscreened graphene plasmon (Fig. 2c) wavepackets on the ZnO gate device schematically shown in Figs. 2a and b. The graphene in this case was 8- μm wide and 23- μm long. Figure 2d shows the time-domain waveform of the THz electrical pulse as a function of the ZnO gate voltage (V_{ZnO} : -3 to 3 V, carrier density n : -6.2 to $7.9 \times 10^{11} \text{ cm}^{-2}$). The time origin ($t = 0$) corresponds to the time at which the THz electrical pulse was applied on the ohmic contact, and the peak position corresponds to the time of flight of the wavepacket through the 23- μm -long graphene micro ribbon (see Supplementary Section I-a for details). For both electron and hole doping, an ultrashort plasmon wavepacket with a peak position around 1-2 ps appears; its amplitude decreases with decreasing carrier density due to increased plasmon propagation loss and impedance mismatch at higher graphene resistivities. Plasmons cannot propagate exactly at the charge neutrality point ($V_{\text{CNP}} = -0.35 \text{ V}$). Note that the small signals around 5 and 9 ps originate from multiple reflections at both ends of the graphene and the PC switches. Now let us examine the propagation characteristics of the plasmon wavepackets by comparing the waveforms normalized by the peak amplitude in the inset of Fig. 2d. With increasing carrier density, the peak position shifts to an earlier time, indicating increase in plasmon velocity. The velocity calculated by dividing the graphene length (23 μm) by the peak position is plotted in Fig. 2e as a function of the carrier density. The velocity increases with doping from 1.5 to $1.8 \times 10^7 \text{ m/s}$. Alongside this velocity change, the pulse duration decreases, reaching 2.0 ps (FWHM) at $V_{\text{ZnO}} = 3.0 \text{ V}$. Despite this shortening, the pulse is still broader than the input pulse (duration of 1.2 ps; Fig. 1b).

To quantitatively understand the changes in the plasmon velocity, we simulated the waveform of graphene plasmon wavepackets by using the dispersion of unscreened graphene plasmons^{1,2} $\omega_p \propto n^{\frac{1}{4}} k^{\frac{1}{2}}$ and the measured waveform of the input electrical pulse (Fig. 1b) (refer to Supplementary Section II for the details of the simulation). Though the

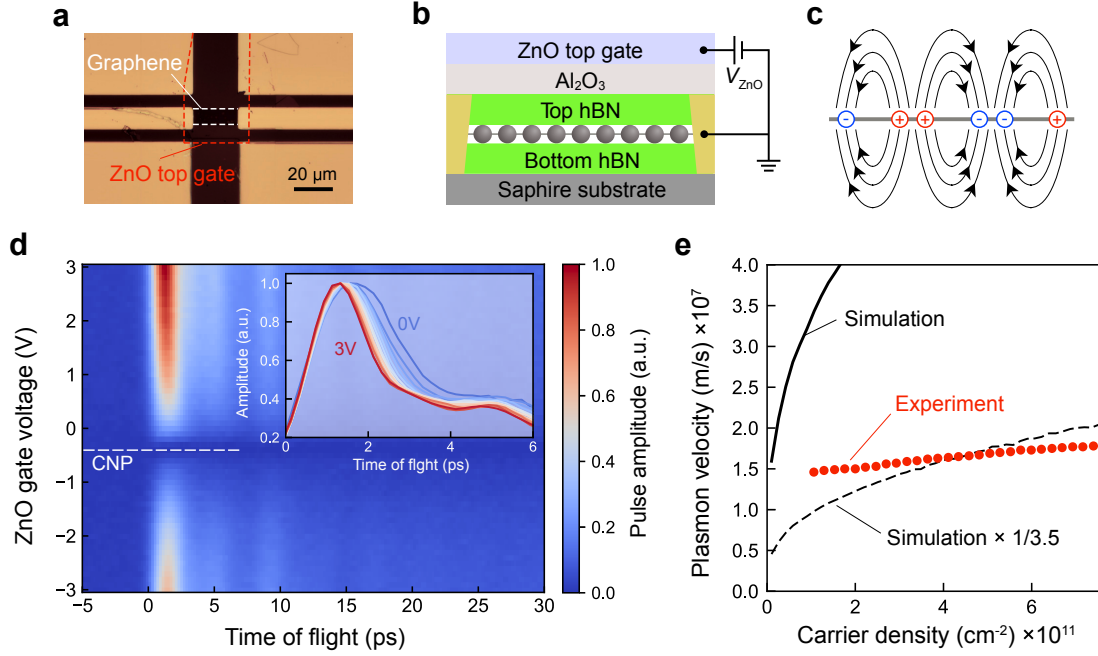


Figure 2 | Unscreened plasmon transport in ZnO gate device. **a**, Optical micrograph depicting the ZnO gate device. The geometric boundaries of the graphene and ZnO top gate are outlined by white and red dashed lines, respectively. **b**, Cross-sectional view of the sample. The transparency of the ZnO top gate to GHz and THz electric fields permits the formation of unscreened graphene plasmons. **c**, Schematic diagram of unscreened graphene plasmon with the associated charge and electromagnetic force. **d**, Time-domain waveforms for various ZnO gate biases. The horizontal dashed line indicates the charge neutrality point ($V_{\text{CNP}} = -0.35$ V). The inset shows normalized time-domain waveforms around the peak position. The pulse duration is 2.0 ps (FWHM) at $V_{\text{ZnO}} = 3.0$ V. **e**, Measured (red circles) and simulated plasmon (solid black curve) velocities as a function of the carrier density. See Supplementary Section II for a detailed explanation of the simulation. The measured velocity is slower than the simulation by roughly 3.5 times and less sensitive to changes in the carrier density, which are attributed to the waveguide mode formation.

simulated wavepackets show qualitatively similar behaviour to the experimentally obtained ones (see the shortening of the pulse duration and increase in velocity with carrier density in Fig. S3), the measured velocity is slower than the simulated value by a factor of around 3.5 and is much less sensitive to changes in the carrier density. These differences can be attributed to formation of a waveguiding mode by lateral confinement in the graphene micro ribbon. According to the finite element simulation in ref.⁴⁴, the

wavelength of THz plasmons in a micro ribbon is predominantly determined by the lateral width of the ribbon, which is consistent with the observed insensitivity of the plasmon velocity to changes in the carrier density. The finite element simulation⁴⁴ also predicts that the plasmon velocity in a graphene micro ribbon is several times slower than that of bulk plasmons below a few THz, which is in agreement with the measurements. These facts demonstrate that we can transfer ultrashort wavepackets of graphene plasmons in a waveguide. Furthermore, we can turn on/off the transfer by switching V_{ZnO} between the values for a large doping and the CNP.

Acoustic graphene plasmons in an Au gate device

Next, we examined the transport properties of graphene plasmons in a device with an Au top gate (Figs. 3a and b). The graphene is 8- μm wide and 26- μm long, and the length of the Au top gate is 12 μm . Owing to the screening effect induced by the Au top gate (Fig. 3c), the plasmon velocity is expected to be reduced significantly compared with the unscreened case, and the dispersion should be a linear relation^{27,28} $\omega_p \propto k$; because of this linearity, the screened plasmon is called an acoustic plasmon. In addition to the Au top gate, we incorporated a ZnO top gate to control the carrier density in the areas between the ohmic contacts and the Au gated regions. This allowed us to control the coupling strength between acoustic plasmons in graphene and the electrical pulse in the CPW (see Fig. S5 of the Supplementary Information). In the subsequent measurements, we kept V_{ZnO} at 3 V in order to achieve a strong coupling. Figure 3d presents the time-domain waveform of the wavepacket as a function of the Au gate voltage (V_{Au} : -2.5 to 0.5 V, n : -5.5 to $7.1 \times 10^{11} \text{ cm}^{-2}$). Note that the secondary peak around 10 ps originates from multiple reflections at both ends of the graphene and the PC switches, whereas our focus is on the first peak around 4 ps. The inset shows a normalized plot highlighting the peak shift near the CNP. Unlike the ZnO gate sample, which exhibits waveguide mode formation, the peak position shifts significantly with the gate voltage in the Au gate sample. Figure 3e shows the plasmon velocity calculated from the peak position and the propagation length determined by the Au gate length (12 μm). The velocity varies from 1.9 to $3.2 \times 10^6 \text{ m/s}$ with doping. These values are close to the Fermi velocity ($\sim 1 \times 10^6 \text{ m/s}$) and are one order of magnitude slower than those in the ZnO gate sample (Fig. 2e). The carrier density dependence of the velocity v_{ac} above $n = 2 \times 10^{11} \text{ cm}^{-2}$ is well reproduced by theory for

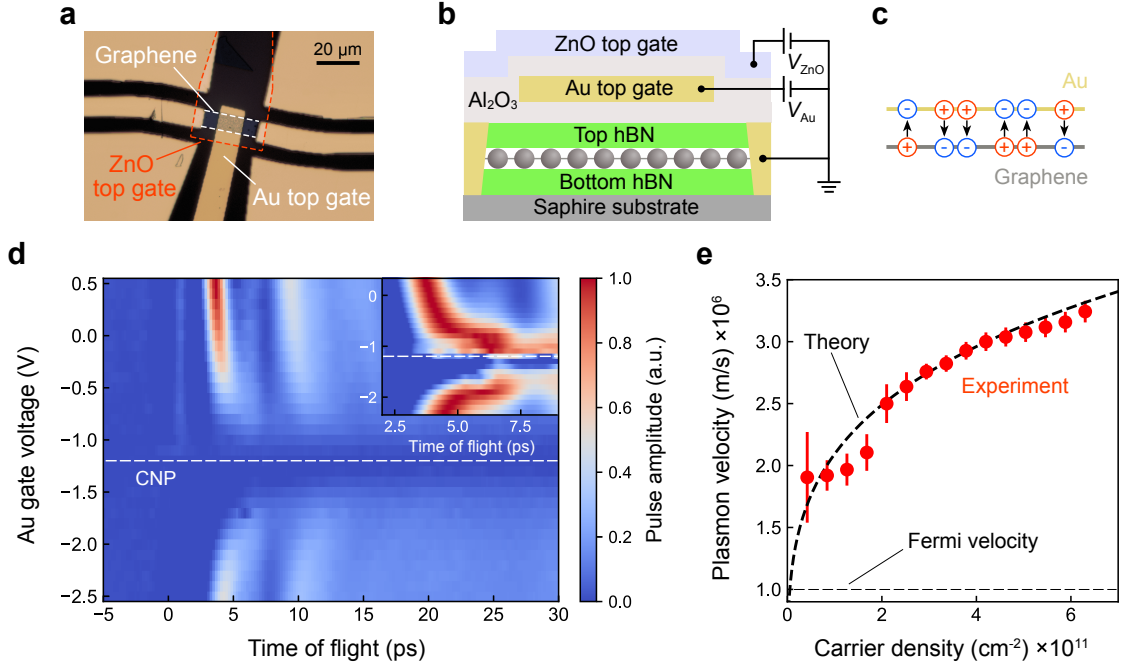


Figure 3 | Acoustic plasmon transport in Au gate device. **a**, Optical micrograph depicting the Au gate device. The geometric boundaries of the graphene and ZnO top gate are outlined by white and red dashed lines, respectively. **b**, Cross-sectional view of the sample. The Au gate is used to induce screening for forming acoustic plasmons. The ZnO gate bias is fixed at a large value, $V_{\text{ZnO}} = 3$ V, to maximize the coupling strength between the electrical pulse in the CPW and plasmons in graphene. **c**, Schematic diagram of acoustic plasmon with the associated charge and electromagnetic force. **d**, Time-domain waveform for various Au gate biases. The horizontal dashed line indicates the charge neutrality point ($V_{\text{CNP}} = -1.2$ V). The inset shows a normalized plot around the peak position. **e**, Measured (red circles) and calculated plasmon (black dashed curve) velocities as a function of carrier density.

the acoustic plasmon⁴⁵ $v_{\text{ac}} \propto n^{\frac{1}{4}}$ (see Supplementary Section III for details). Note that this agreement, coupled with the significant tunability of velocity with carrier density, suggests that the waveguide mode does not form in the Au gate sample. The absence of a waveguiding mode can be attributed to the fact that the characteristic size of the field distribution of the acoustic plasmon, determined by the separation of the graphene and Au gate (65 nm) and the plasmon wavelength (~ 2.5 μm at 1 THz), is much smaller than the width of the graphene micro ribbon (8 μm). On the other hand, the measured velocity deviates from the theoretical value for densities below $n = 2 \times 10^{11}$ cm^{-2} due to dissipation

as discussed below.

Coherent and incoherent transport of ultrashort wave packet

For a comprehensive understanding of the transport properties of the acoustic plasmon, let us analyse the time-domain waveform in the n -doped region (Fig. 4a). Remarkably, the measured waveform at $V_{Au} = 1.5$ V ($n = 11.3 \times 10^{11}$ cm $^{-2}$) has a pulse duration of 1.2 ps (FWHM). To the best of our knowledge, this is the shortest electrically generated plasmon wavepacket on a material. It propagates with a velocity of 3.3×10^6 m/s and is directionally confined to 4.0 μ m. Together with the vertical confinement of 65 nm (30 nm Al $_2$ O $_3$ layer and 35 nm hBN layer) due to the screening effect and the lateral confinement of 8 μ m due to the width of the graphene, this means that the plasmon wavepacket is

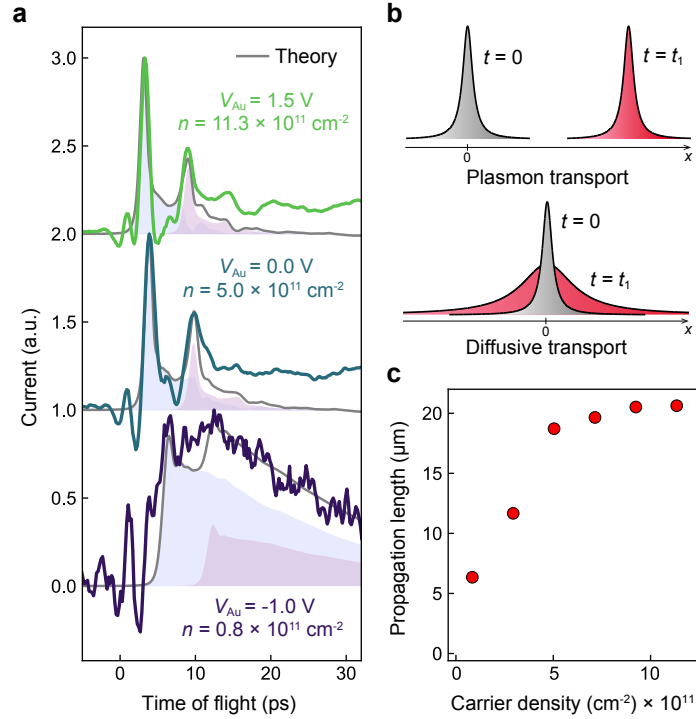


Figure 4 | Waveform comparison between experiment and theory. **a**, Experimental (colored traces) and simulated (gray traces) normalized time-domain waveforms of wavepackets for three Au gate biases. The simulation includes the initial (blue area) and the first echo (purple area) pulses (see Supplementary Section III for details). Each waveform is offset by unity for clarity. **b**, Schematic diagram of wavepacket transport in real space in the different transport regimes. **c**, Simulated propagation length of acoustic plasmon wavepackets as a function of the carrier density obtained by the telegrapher's equation⁴⁵.

confined within a $2.1 \times 10^{-18} \text{ m}^3$ volume. The volume normalized by free space wavelength (calculated from the center frequency of 0.28 THz obtained from the inset of Fig. 1b and the speed of light of $3 \times 10^8 \text{ m/s}$) is 5.2×10^{-9} . This extremely tight confinement would be beneficial for constructing various graphene plasmonic nanocircuits. It is worth noting that the width of 1.2 ps for the plasmon wavepacket is the same as that of the input electrical pulse, which is consistent with the linear dispersion of the acoustic plasmon. As the carrier density is decreased, the pulse duration becomes longer than 20 ps at $V_{\text{Au}} = -1.0 \text{ V}$ ($n = 0.8 \times 10^{11} \text{ cm}^{-2}$). The range of carrier densities exhibiting this pulse broadening corresponds to the range where the velocity deviates from the theoretical acoustic plasmon velocity (Fig. 3e).

The evolution of the waveform with carrier density can be explained by a simulation solving the telegrapher's equation for an *RLC* distributed constant circuit^{33,45}, where *R*, *L*, and *C* correspond to the resistivity of graphene, graphene kinetic inductance, and capacitance between graphene and the Au gate (for details, refer to Supplementary Section III). The initial and the first echo pulse from the PC switches are included in the simulation. The simulation accurately reproduces the experimental waveform, including the pulse width and the peak position, for the whole carrier density range. The solution to the telegrapher's equation⁴⁵ suggests that crossover from coherent plasmonic transport to incoherent diffusive transport (Fig. 4b) occurs as the carrier density is decreased to the CNP. In the heavily doped region ($V_{\text{Au}} = 1.5 \text{ V}$), the wavepacket traverses the graphene in a coherent manner as acoustic plasmons. Hence, the pulse duration remains identical to the input electrical pulse. Conversely, near the CNP ($V_{\text{Au}} = -1.0 \text{ V}$), where the resistivity is high, the acoustic plasmon dissipates before traveling $12 \text{ }\mu\text{m}$ due to the shorter lifetime, leading to a broader pulse through incoherent diffusive transport. Since diffusive transport is much slower than plasmon transport, the peak of the waveform shifts with a longer time delay when diffusive transport becomes dominant near the CNP.

With this model, we can deduce the propagation length of acoustic plasmons (Fig. 4c). At the highest doping level, the propagation length l_p reaches $21 \text{ }\mu\text{m}$. With a pulse width of $4.0 \text{ }\mu\text{m}$, more than five wavepackets can be transferred before decoherence. Notably, this exceeds the previously reported value of 2.1, obtained with a plasmonic wavelength of 222 nm and $l_p = 470 \text{ nm}$, which was measured using near-field scanning optical microscopy on CVD graphene at room temperature³¹. Since our model predicts that the

propagation length scales inversely with resistivity, $l_p \propto 1/R$, further improvements to the carrier mobility through optimization of the device fabrication process could lead to an even greater l_p .

Efficiency of conversion between electrical pulse and graphene plasmon

Finally, let us discuss the efficiency of conversion between the electrical pulse and the graphene plasmon wavepacket. We expected that the electrical excitation used in this study would have high conversion efficiency as it bypasses some of the restrictions associated with optical excitations, such as substantial momentum mismatches^{15–32} and graphene's small nonlinear coefficient⁴⁶. To demonstrate this, we plotted the time-domain waveform of the unscreened and acoustic plasmon wavepackets together with the input

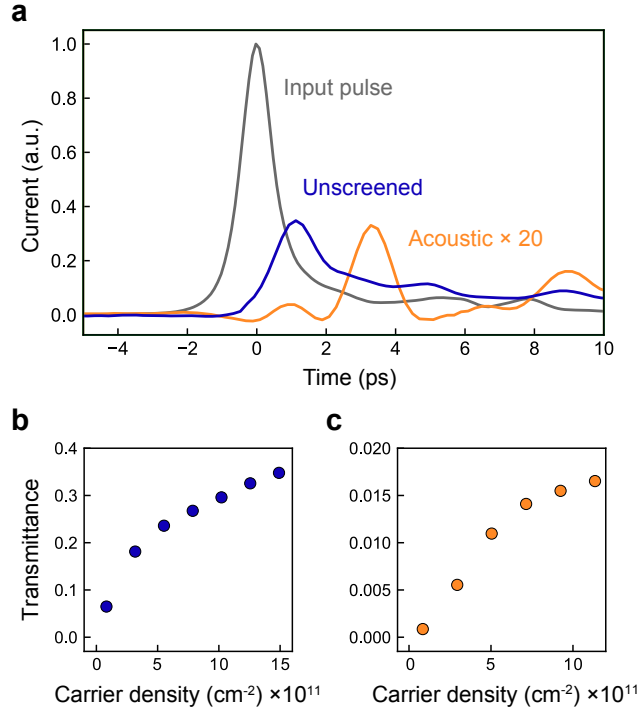


Figure 5 | Conversion efficiency for graphene plasmons. **a**, Time-domain waveform of input electrical pulse together with the unscreened (ZnO gate: $n = 15.0 \times 10^{11} \text{ cm}^{-2}$) and acoustic (Au gate: $n = 11.3 \times 10^{11} \text{ cm}^{-2}$) graphene plasmon wavepackets. The amplitude of the wavepacket is normalized to the peak amplitude of the input pulse. The amplitude of the acoustic plasmon is magnified by a factor of 20 for clarity. **b,c**, Transmittance of the unscreened (**b**) and acoustic (**c**) graphene plasmon as a function of the carrier density. Transmittance is the ratio of the peak amplitude to that of the input pulse.

electrical pulse with the amplitude normalized relative to the input electrical pulse (Fig. 5a); for the normalization, the responsivity of the PC switches was adjusted (see Supplementary Section I-b). Figures 5b and c show the transmittance, defined as the ratio of the peak amplitudes $I_{\text{out}}/I_{\text{input}}$ of the input and output electrical pulses. This transmittance value is affected by the following three processes: (1) conversion of the input electrical pulse into the graphene plasmon wavepacket ($I_{\text{input}} \rightarrow I_{\text{plasmon}}$); (2) attenuation of the plasmon wavepacket as it moves within the graphene; (3) conversion of the plasmon wavepacket into the output electrical pulse ($I_{\text{plasmon}} \rightarrow I_{\text{output}}$). Given that processes (1) and (3) take place at CPW-graphene interfaces under identical conditions ($I_{\text{plasmon}}/I_{\text{input}} = I_{\text{output}}/I_{\text{plasmon}}$), the transmittance provides a lower bound for the energy conversion efficiency, $\eta = (I_{\text{plasmon}}/I_{\text{input}})^2$. Namely, $I_{\text{out}}/I_{\text{input}} = (I_{\text{plasmon}}/I_{\text{input}})^2 \zeta = \eta \zeta$, where $\zeta (\leq 1)$ is the plasmon attenuation in process (2). For unscreened plasmons, η can exceed 0.35 at high carrier densities. For acoustic plasmons, since the propagation length is 21 μm , $\zeta \sim 0.56$ and η can be as large as 0.03. These values are orders of magnitude higher than the previously reported $\eta = 6 \times 10^{-5}$ for optical excitation of propagating THz graphene plasmons⁴⁶. These unusually high conversion efficiencies come from the fact that energy losses due to momentum mismatches are absent for the conversion between the electrical pulse and the plasmon wavepacket. Instead, we suggest that the high-frequency impedance mismatch between the CPW and the graphene transistor is a limiting factor in our devices. In the Au gate device, the large difference in velocity between the electrical pulse in the CPW ($\sim 1 \times 10^8$ m/s) and the acoustic plasmon ($\sim 3 \times 10^6$ m/s) and also the presence of the Au gate induce a large impedance mismatch. In the ZnO gate device, on the other hand, the smaller velocity difference due to the higher plasmon velocity ($\sim 1 \times 10^7$ m/s) and the transparent ZnO gate in the THz range result in a smaller impedance mismatch and thus a higher conversion efficiency. It is important to note that the frequency component of the plasmon wavepacket transferred from the input electrical pulse covers a broad frequency range. Our ability to produce propagating plasmons over a wide frequency range with significant efficiency will be pivotal to the development of graphene plasmonic circuitry⁵⁻¹². We foresee the potential for further enhancement of the conversion efficiency, for instance, by constructing subwavelength structures that reduce the impedance mismatch between the CPW and the graphene transistor.

Discussion

Using newly developed THz electronics, we demonstrated on-chip generation, manipulation, and detection of ultrashort graphene plasmon wavepackets. Through injection of an ultrashort electrical pulse into a graphene micro ribbon via an ohmic contact and manipulation of the dielectric environment with ZnO and Au top gates, we were able to uncover transport properties of unscreened and acoustic graphene plasmon wavepackets within the THz regime. These insights were obtained from precise measurements of the time-domain waveform. The unscreened plasmons in the ZnO gate device had a velocity on the order of 10^7 m/s, with waveguiding modes forming due to the lateral confinement afforded by the graphene micro ribbon. On the other hand, the velocity of the acoustic plasmons in the Au gate device dropped by an order of magnitude to 10^6 m/s. At high carrier densities, the injected wavepackets propagated coherently as acoustic plasmons with a minimum pulse width of 1.2 ps. Conversely, they diffused incoherently near the CNP, resulting in a broader pulse. Remarkably, the shortest wavepacket was tightly confined within a tiny volume, 2.1×10^{-18} m³, making acoustic plasmons an ideal candidate for constructing graphene plasmonic nanocircuits. The propagation length of acoustic plasmons was estimated to be 21 μ m by waveform analysis and is the longest value reported to date. Furthermore, our method yielded a high conversion efficiency between electrical pulses and plasmon wavepackets, reaching $\eta = 0.35$ and 0.03 for unscreened and acoustic plasmons, respectively. This level of efficiency is a significant improvement over those achieved with optical excitation of propagating graphene plasmon wavepackets and thus highlights the advantages of our excitation scheme utilizing spatiotemporally localized electrical pulses. By overcoming the limitations of conventional optical techniques, our findings and methods for handling graphene plasmon wavepackets, all on-chip, will serve as a new guideline for constructing plasmonic circuits for information transfer and processing.

We also suggest that the ability to excite and measure electrical pulses as short as 1.2 ps will be pivotal for investigating and manipulating the transport properties of various quantum materials and circuits besides graphene, such as van der Waals heterostructures composed of two-dimensional materials³⁻⁵ and quantum nanoelectronic devices⁴⁷⁻⁵⁰. The use of THz electronics as a means of shrinking the pulse duration by more than one order

of magnitude of that achievable by conventional GHz electronics⁵⁰ will facilitate the development of a new field of study in which the size of plasmon or single-electron wavepackets^{47–50} is significantly smaller than the material size and coherence length. We envision that our THz-electronics approach will accelerate the progress of polariton studies in van der Waals heterostructures and electron quantum optics in various quantum nanocircuits and will unlock new capabilities for controlling ultrafast signals on-chip.

References

1. Grigorenko, A. N., Polini, M. & Novoselov, K. S. Graphene plasmonics. *Nat. Photonics* **6**, 749–758 (2012).
2. Low, T. & Avouris, P. Graphene Plasmonics for Terahertz to Mid-Infrared Applications. *ACS Nano* **8**, 1086–1101 (2014).
3. Basov, D. N., Fogler, M. M. & García de Abajo, F. J. Polaritons in van der Waals materials. *Science* **354**, aag1992–aag1992 (2016).
4. Low, T. *et al.* Polaritons in layered two-dimensional materials. *Nat. Mater.* **16**, 182–194 (2017).
5. Zhang, Q. *et al.* Interface nano-optics with van der Waals polaritons. *Nature* **597**, 187–195 (2021).
6. Vakil, A. & Engheta, N. Transformation Optics Using Graphene. *Science* **332**, 1291–1294 (2011).
7. Ooi, K. J. A., Chu, H. S., Bai, P. & Ang, L. K. Electro-optical graphene plasmonic logic gates. *Opt. Lett.* **39**, 1629 (2014).
8. Wu, X., Tian, J. & Yang, R. A type of all-optical logic gate based on graphene surface plasmon polaritons. *Opt. Commun.* **403**, 185–192 (2017).
9. Jin, D. *et al.* Infrared Topological Plasmons in Graphene. *Phys. Rev. Lett.* **118**, 245301 (2017).
10. Gullans, M., Chang, D. E., Koppens, F. H. L., de Abajo, F. J. G. & Lukin, M. D. Single-Photon Nonlinear Optics with Graphene Plasmons. *Phys. Rev. Lett.* **111**, 247401 (2013).
11. Alonso Calafell, I. *et al.* Quantum computing with graphene plasmons. *npj Quantum Inf.* **5**, 37 (2019).
12. Calajó, G. *et al.* Nonlinear quantum logic with colliding graphene plasmons.

- Phys. Rev. Res.* **5**, 1–12 (2023).
13. Fang, Y. & Sun, M. Nanoplasmonic waveguides: Towards applications in integrated nanophotonic circuits. *Light Sci. Appl.* **4**, 1–11 (2015).
 14. Davis, T. J., Gómez, D. E. & Roberts, A. Plasmonic circuits for manipulating optical information. *Nanophotonics* **6**, 543–559 (2017).
 15. Ju, L. *et al.* Graphene plasmonics for tunable terahertz metamaterials. *Nat. Nanotechnol.* **6**, 630–634 (2011).
 16. Gao, W. *et al.* Excitation and Active Control of Propagating Surface Plasmon Polaritons in Graphene. *Nano Lett.* **13**, 3698–3702 (2013).
 17. Yeung, K. Y. M. *et al.* Far-Infrared Graphene Plasmonic Crystals for Plasmonic Band Engineering. *Nano Lett.* **14**, 2479–2484 (2014).
 18. Poumirol, J.-M. *et al.* Electrically controlled terahertz magneto-optical phenomena in continuous and patterned graphene. *Nat. Commun.* **8**, 14626 (2017).
 19. Alcaraz Iranzo, D. *et al.* Probing the ultimate plasmon confinement limits with a van der Waals heterostructure. *Science* **360**, 291–295 (2018).
 20. Lee, I.-H., Yoo, D., Avouris, P., Low, T. & Oh, S.-H. Graphene acoustic plasmon resonator for ultrasensitive infrared spectroscopy. *Nat. Nanotechnol.* **14**, 313–319 (2019).
 21. Epstein, I. *et al.* Far-field excitation of single graphene plasmon cavities with ultracompressed mode volumes. *Science* **368**, 1219–1223 (2020).
 22. Tu, N. H. *et al.* Active spatial control of terahertz plasmons in graphene. *Commun. Mater.* **1**, 7 (2020).
 23. Huang, T. *et al.* Observation of chiral and slow plasmons in twisted bilayer graphene. *Nature* **605**, 63–68 (2022).
 24. Fei, Z. *et al.* Gate-tuning of graphene plasmons revealed by infrared nano-imaging. *Nature* **487**, 82–85 (2012).
 25. Fei, Z. *et al.* Electronic and plasmonic phenomena at graphene grain boundaries. *Nat. Nanotechnol.* **8**, 821–825 (2013).
 26. Ni, G. X. *et al.* Plasmons in graphene moiré superlattices. *Nat. Mater.* **14**, 1217–1222 (2015).
 27. Alonso-González, P. *et al.* Acoustic terahertz graphene plasmons revealed by

- photocurrent nanoscopy. *Nat. Nanotechnol.* **12**, 31–35 (2017).
28. Lundeberg, M. B. & Hillenbrand, R. Tuning quantum nonlocal effects in graphene plasmons. *Science* **191**, 187–191 (2017).
 29. Ni, G. X. *et al.* Fundamental limits to graphene plasmonics. *Nature* **557**, 530–533 (2018).
 30. Sunku, S. S. *et al.* Photonic crystals for nano-light in moiré graphene superlattices. *Science* **362**, 1153–1156 (2018).
 31. Menabde, S. G. *et al.* Real-space imaging of acoustic plasmons in large-area graphene grown by chemical vapor deposition. *Nat. Commun.* **12**, 938 (2021).
 32. Utama, M. I. B., Kahn, S., Jiang, Y., Xiao, X. & Yoo, S. Efficient Fizeau drag from Dirac electrons in monolayer graphene. *Nature* **594**, (2021).
 33. Kumada, N. *et al.* Plasmon transport and its guiding in graphene. *New J. Phys.* **16**, 063055 (2014).
 34. Petković, I. *et al.* Carrier Drift Velocity and Edge Magnetoplasmons in Graphene. *Phys. Rev. Lett.* **110**, 016801 (2013).
 35. Kumada, N. *et al.* Plasmon transport in graphene investigated by time-resolved electrical measurements. *Nat. Commun.* **4**, 1363–1366 (2013).
 36. Kumada, N. *et al.* Resonant Edge Magnetoplasmons and Their Decay in Graphene. *Phys. Rev. Lett.* **113**, 266601 (2014).
 37. Prechtel, L. *et al.* Time-resolved ultrafast photocurrents and terahertz generation in freely suspended graphene. *Nat. Commun.* **3**, 646 (2012).
 38. Wu, J. *et al.* Excitation, detection and electrostatic manipulation of terahertz-frequency range plasmons in a two-dimensional electron system. *Sci. Rep.* **5**, 15420 (2015).
 39. Island, J. O. *et al.* On-chip terahertz modulation and emission with integrated graphene junctions. *Appl. Phys. Lett.* **116**, 161104 (2020).
 40. McIver, J. W. *et al.* Light-induced anomalous Hall effect in graphene. *Nat. Phys.* **16**, 38–41 (2020).
 41. Yoshioka, K. *et al.* Ultrafast intrinsic optical-to-electrical conversion dynamics in a graphene photodetector. *Nat. Photonics* **16**, 718–723 (2022).
 42. Zhao, W. *et al.* Observation of hydrodynamic plasmons and energy waves in graphene. *Nature* **614**, 688–693 (2023).

43. Wang, L. *et al.* One-Dimensional Electrical Contact to a Two-Dimensional Material. *Science* **342**, 614–617 (2013).
44. Nikitin, A. Y., Guinea, F., García-Vidal, F. J. & Martín-Moreno, L. Edge and waveguide terahertz surface plasmon modes in graphene microribbons. *Phys. Rev. B* **84**, 161407 (2011).
45. Sasaki, K. & Kumada, N. Effects of screening on the propagation of graphene surface plasmons. *Phys. Rev. B* **90**, 035449 (2014).
46. Yao, B. *et al.* Broadband gate-tunable terahertz plasmons in graphene heterostructures. *Nat. Photonics* **12**, 22–28 (2018).
47. Bocquillon, E. *et al.* Coherence and Indistinguishability of Single Electrons Emitted by Independent Sources. *Science* **339**, 1054–1057 (2013).
48. Dubois, J. *et al.* Minimal-excitation states for electron quantum optics using levitons. *Nature* **502**, 659–663 (2013).
49. Bäuerle, C. *et al.* Coherent control of single electrons: a review of current progress. *Reports Prog. Phys.* **81**, 056503 (2018).
50. Aluffi, M. *et al.* Ultrashort Electron Wave Packets via Frequency-Comb Synthesis. *Phys. Rev. Appl.* **20**, 034005 (2023).

Methods

Device fabrication

Photoconductive switches were prepared using an LT-GaAs wafer supplied by BATOP, GmbH. The wafer consisted of a 2.6- μm -thick LT-GaAs surface layer (grown at 300 °C) and a 500-nm-thick $\text{Al}_{0.9}\text{Ga}_{0.1}\text{As}$ sacrificial layer on a semi-insulating GaAs substrate. After the LT-GaAs layer was etched into 100 μm \times 100 μm squares by using a citric acid solution, the sacrificial layer was dissolved in hydrochloric acid. The etched LT-GaAs chips on the GaAs substrate were transferred to a sapphire substrate by using a thermoplastic methacrylate copolymer (Elvacite 2552C, Lucite International) as an adhesive⁵¹. The remaining Elvacite on the sapphire substrate was removed with citric acid.

Graphene was prepared via mechanical exfoliation of natural graphite on silica (285 nm)/doped silicon substrates. Monolayer graphene was identified via optical contrast under a microscope. Using a separately exfoliated hBN flake, graphene was picked up and transferred onto the sapphire substrate by using the dry-transfer technique with

polydimethylsiloxane and polycarbonate⁴⁴. The thickness of the hBN layer on top of the graphene was 72 nm for the ZnO gate device and 35 nm for the Au gate device. The carrier mobility within the graphene, measured at 4 K, was 250,000 cm²V⁻¹s⁻¹ for the ZnO gate device and 73,000 cm²V⁻¹s⁻¹ for the Au gate device.

The graphene was patterned by reactive ion etching, and the Ti/Au waveguide structure with side contacts to graphene was deposited by sputtering. The whole surface was covered with a 30-nm-thick alumina (Al₂O₃) insulating layer grown by atomic layer deposition. For the Au gate device, Ti/Au (10/100 nm) was patterned on the Al₂O₃ layer by using photolithography, deposition, and lift-off processes. Then, for both devices, a 20-nm-thick ZnO gate was grown and patterned by using atomic layer deposition at 200°C. The ZnO gate was protected by another Al₂O₃ layer deposited on top. Finally, in order to make electrical contact with the waveguide, Miroposit 351 developer was used to remove the Al₂O₃ on the bonding pads.

On-chip THz spectroscopy measurements

A femtosecond laser (Monaco, Coherent, Ltd.) was used as the light source (1,035 nm, 280 fs, 50 MHz). Two orthogonally polarized pump and probe beams were combined using a polarization beam splitter and aligned with a slight displacement in order to focus them onto the two LT-GaAs PC switches by using an objective lens⁵² for generation and detection of ultrashort electrical currents. The pump power was 20 mW for both PC switches, and a 30 V bias was applied to the injection PC switch. An optical chopper modulated the pump beam at a few hundred hertz for lock-in detection of the terahertz current.

Measured plasmon signals have crosstalk. The crosstalk component can be determined at the CNP, where plasmons cannot propagate. Since the crosstalk is independent of the graphene carrier density, plasmon signals free from the crosstalk can be obtained by subtracting the signal at the CNP from those at finite carrier densities.

References

51. Masubuchi, S. *et al.* Autonomous robotic searching and assembly of two-dimensional crystals to build van der Waals superlattices. *Nat. Commun.* **9**, 1413 (2018).

52. Yoshioka, K., Kumada, N., Muraki, K. & Hashisaka, M. On-chip coherent frequency-domain THz spectroscopy for electrical transport. *Applied Physics Letters* **117**, 161103 (2020).

Data availability

The datasets generated during and/or analysed during the current study are available from the corresponding author on reasonable request.

Acknowledgements

The authors thank H. Murofushi for technical support. K.W. and T.T. acknowledge support from the JSPS KAKENHI (Grant Numbers 21H05233 and 23H02052) and World Premier International Research Center Initiative (WPI), MEXT, Japan.

Author contributions

K.Y. and N.K. conceived the experiment. K.Y. and G.B. designed and built the optical setup, performed the measurement, analysed the data, and conducted the unscreened plasmon simulation. K. S. simulated the acoustic plasmon wavepacket. K.Y., G.B. and N.K. designed the THz circuits with support from T.W. and M.H. G. B., T.W., S.S. and N.K. fabricated the devices. K.W. and T.T. contributed the hBN material. K.Y. and N.K. wrote the paper, with input from all authors.

Competing financial interests

The authors declare no competing financial interests.

Supplementary Information for

On-chip transfer of ultrashort graphene plasmon wavepackets using terahertz electronics

Katsumasa Yoshioka^{1,*}, Guillaume Bernard¹, Taro Wakamura¹, Masayuki Hashisaka¹, Ken-ichi Sasaki¹, Satoshi Sasaki¹, Kenji Watanabe², Takashi Taniguchi³, and Norio Kumada¹

¹NTT Basic Research Laboratories, NTT Corporation, Atsugi, 243-0198, Japan

²Research Center for Electronic and Optical Materials, National Institute for Materials Science, Tsukuba, Japan

³Research Center for Materials Nanoarchitectonics, National Institute for Materials Science, Tsukuba, Japan

*e-mail: katsumasa.yoshioka@ntt.com

I-a. Determining time origin and propagation velocity

In our on-chip THz spectroscopy, the peak of the THz current signals the moment when the travel time of the generated wavepacket between the two photoconductive (PC) switches matches the time delay of the probe beam from the pump beam (Fig. S1a). The point at which the pump and probe beams arrive simultaneously is the midpoint of the two wavepackets and it is determined by switching the pump and probe PC switches (Fig. S1b). The propagation velocity in the coplanar waveguide (CPW) is then calculated for a device without graphene by dividing the distance between Switch A and B by the time delay at the current peak. The calculated propagation velocity is $v_{CPW} = 1.20 \times 10^8$ m/s, in good agreement with the literature value¹. The time used in the main manuscript is

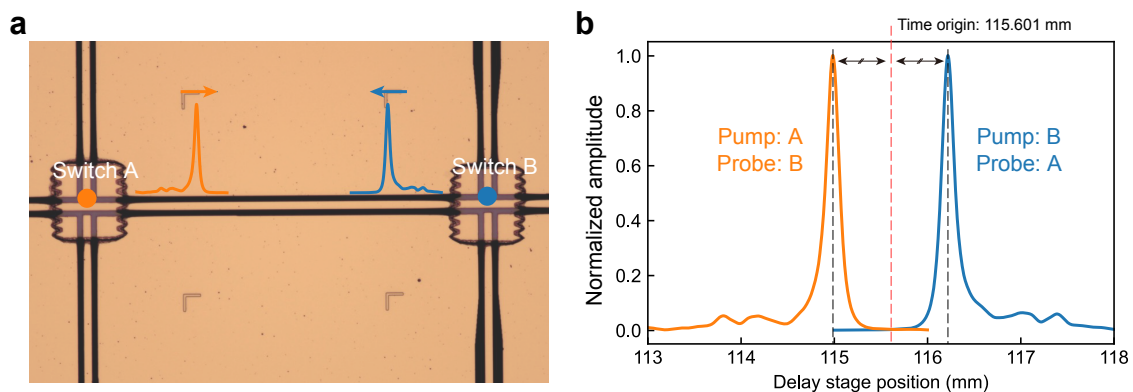


Figure S1 | Pump switching experiment in a coplanar waveguide. **a**, Optical micrograph of a CPW. The distance between PC switches is 485 μm. **b**, Normalized waveform obtained by pumping different PC switches A and B. Corresponding pump spot positions are depicted with coloured circles in **a**.

obtained by eliminating the propagation time in the CPW calculated using v_{CPW} and the length of the CPW from the full time delay.

I-b. Calibration of PC switch sensitivity

Our PC switches were fabricated from the same low-temperature-grown gallium arsenide (LT-GaAs) wafer, ensuring a uniform response time across all devices. However, as shown in Fig. S2a, there are variations in responsivity to incident femtosecond laser pulses between different PC switches. (Switches A and B in Fig. S2a are the same as those shown in Fig. S1a). This difference in I-V characteristics originates from minor variations in the contact resistance of the readout electrode and the gap length of the PC switches. The impact of these differences on the measured THz currents is illustrated in Fig. S2b. Here, the excitation conditions, such as the DC bias voltage (30 V) applied to the pump switch, as well as the optical spot size and power, were kept constant. As anticipated, the dynamic response between the two waveforms remains the same. However, the signal amplitude of the configuration with Pump: A, Probe: B (orange) exhibits a signal 50% smaller than that of the other configuration (blue). This confirms that the pump and probe switches have different effects on the measured THz signals.

For the pump switch, the generated current amplitude is determined by the DC current amplitude at 30 V, as the amount of integrated DC current is directly related to the peak

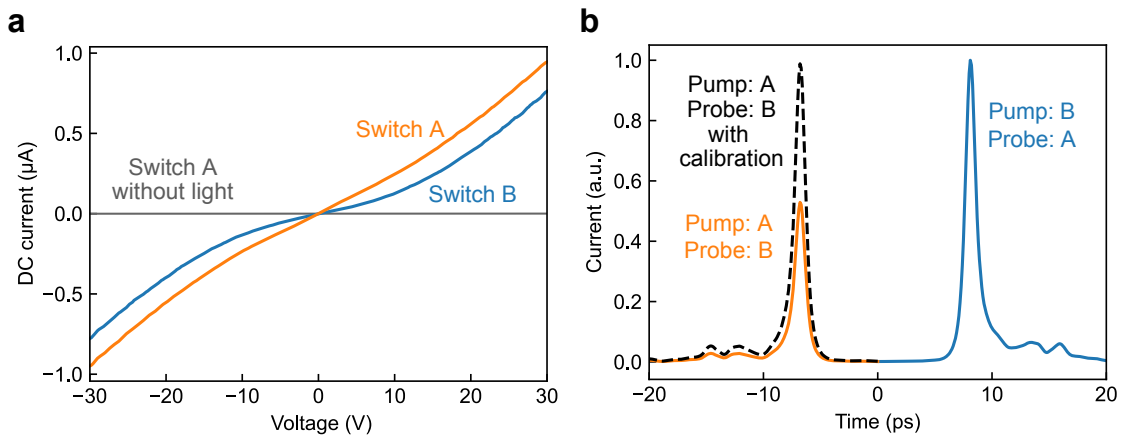


Figure S2 | Calibrating the amplitude of the measured THz current. a, I-V characteristic of PC switches A and B upon femtosecond laser excitation. Both switches exhibit insulating behaviour without laser excitation under the experimental condition at 4 K. **b**, Measured THz current. The amplitude of the THz current can be calibrated using the I-V characteristics of the pump and probe PC switches.

amplitude of the generated THz current. For the probe switch, the readout sensitivity is determined by the slope of the I-V curve in the linear regime (-5 to 5 V). This is because the amplitude of the probe current is determined by the driven photocurrent due to the small voltage of the generated THz current propagating through the CPW. By taking these different I-V characteristics into account, we can calibrate the current amplitude of the measured THz current as shown in Fig. S2b (black dashed curve). This calibration verifies that, after determining the light-excited I-V curves for the pump and probe PC switches, the amplitude of the THz current can be compared across different devices, as in Fig. 5a-c of the main text.

II. Simulation of unscreened graphene plasmon

Figure S3a shows the calculated dispersions of unscreened graphene plasmons in the THz regime obtained by considering them to be a 2-dimensional Dirac plasma². The slope of the dispersion gets steeper as the carrier density increases. With these dispersion relations and measured waveform of the input THz electrical pulse (identical to the waveform displayed in Fig. 1b of the main text), we simulated the waveform of unscreened graphene plasmon wavepackets after 23- μm propagation (Fig. S3b). By increasing the carrier density, the velocity increases, and the pulse duration shortens. This trend qualitatively

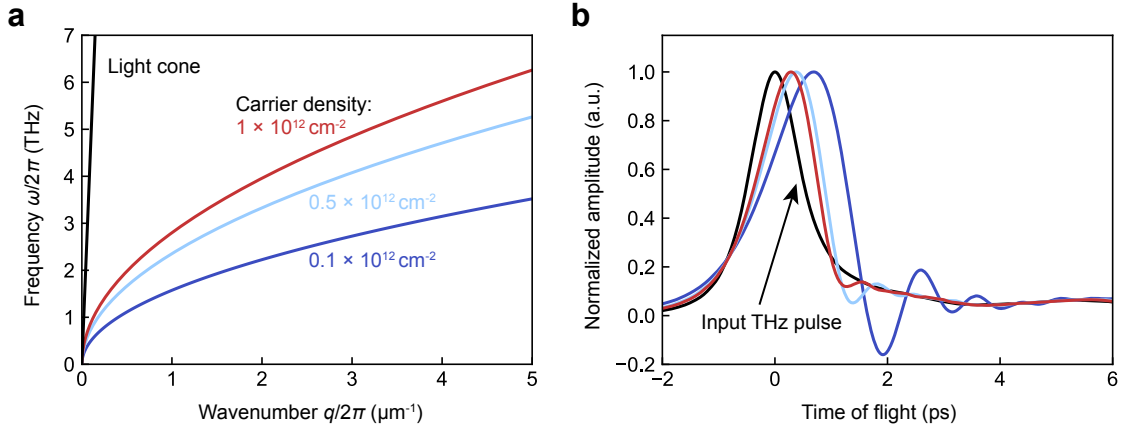


Figure S3 | Simulated waveforms of unscreened graphene plasmon. **a**, Calculated dispersions of unscreened graphene plasmon for different carrier densities. **b**, Simulated waveforms of unscreened graphene plasmon. The color of the waveforms corresponds to the dispersion used for the simulation in **a**. Simulated plasmon velocity (Fig. 2e in the main text) is calculated for the positions of the peaks of these wavepackets.

aligns with the experimental data presented in the inset of Fig. 2d in the main text. However, as discussed in the main text, the experimental velocity is slower by several times than the simulated value due to the formation of a plasmonic waveguide in the graphene micro ribbon³.

III. Simulation of acoustic plasmons

The velocity of acoustic plasmons in graphene shown in Fig. 3e of the main text is theoretically obtained by neglecting the finite resistance of graphene,⁴

$$v_{ac} = 2e \left(\frac{v_F}{C\hbar} \right)^{\frac{1}{2}} (\pi n)^{\frac{1}{4}}, \quad (\text{S1})$$

where e , v_F , C , n correspond to the electron charge, Fermi velocity, capacitance between graphene and the Au gate, and carrier density. Experimental results are well reproduced by Eq. (S1) with $C = 9.7 \times 10^{-4} \text{ Fm}^{-2}$, which is in good agreement with the geometrical capacitance, $C_d = 6.7 \pm 1.8 \times 10^{-4} \text{ Fm}^{-2}$.

The waveform of acoustic plasmons in an actual graphene device with finite resistance can be obtained by using a distributed constant circuit model⁵. The response of charge carriers in graphene to a high-frequency electric field is characterized by the impedance $Z_{\text{graphene}} = R + i\omega L$, where L is the kinetic inductance arising from the inertia of the charge carriers. Since the carrier dynamics depends on n , L can be modified by changing n as $L = \hbar/4v_F e^2 \sqrt{\pi n}$. Including the capacitive coupling to the metal gate C , the wave equation in the propagation direction x can be written in the form of the telegrapher's equation,

$$\left(\frac{\partial^2}{\partial t^2} - \frac{1}{LC} \frac{\partial^2}{\partial x^2} + \frac{R}{L} \frac{\partial}{\partial t} \right) V(x, t) = 0, \quad (\text{S2})$$

where V is the potential induced by excess carriers in graphene. This gives the plasmon dispersion,

$$\omega = \sqrt{\frac{k^2}{LC} - \frac{R^2}{4L^2}}. \quad (\text{S3})$$

Note that Eq. (S3) gives the velocity $v = 1/\sqrt{LC}$ for $R = 0$, which corresponds to Eq. (S1). Furthermore, from the solution to Eq. (S2), the propagation length l_p of the acoustic plasmon can be determined as

$$l_p = \left(\frac{R}{2} \sqrt{\frac{C}{L}} \right)^{-1}. \quad (\text{S4})$$

To compare with the experimental waveform (Fig. 4a in the main text), we performed a numerical simulation of the wavepacket by discretizing the telegrapher's equation, Eq.

(S2), with a square lattice network in graphene. The square lattice network consists of RLC circuit elements shown in the inset of Fig. S4a. At the i -th site of the network, the potential $V_i(t)$ is defined as a function of time t . The Au gate is taken into account by C at each site. The link between nearest-neighbor sites (separation is $\Delta x = 0.5 \mu\text{m}$) consists of L and R connected in a series. The current from site j to i , $I_{j \rightarrow i}(t)$, follows the equations of motion,

$$V_j(t) - V_i(t) = L \frac{I_{j \rightarrow i}(t + \Delta t) - I_{j \rightarrow i}(t)}{\Delta t} + R I_{j \rightarrow i}(t), \quad (\text{S5})$$

$$\sum_{j \neq i}^{nn} I_{j \rightarrow i}(t) = C \frac{V_i(t + \Delta t) - V_i(t)}{\Delta t}. \quad (\text{S6})$$

We used a measured waveform of the input THz electrical pulse (Fig. 1b of the main text) as the driving voltage at the injection site and simulated the time evolution of the plasmon electric field using Eqs. (S5) and (S6). Figure S4a shows a snapshot of the plasmon potential at a time delay of 2 ps. We used $C = 9.7 \times 10^{-4} \text{ Fm}^{-2}$ (same as in the velocity calculation) and $L = \hbar/4v_F e^2 \sqrt{\pi n}$. The value of R used in the simulation corresponds to the DC resistance measurement, as shown in Fig. S4b. Consequently, the waveform simulation requires no adjustable parameters. In addition to the initial pulse, we include the first echo pulse that arises from multiple reflections at the generation and detection

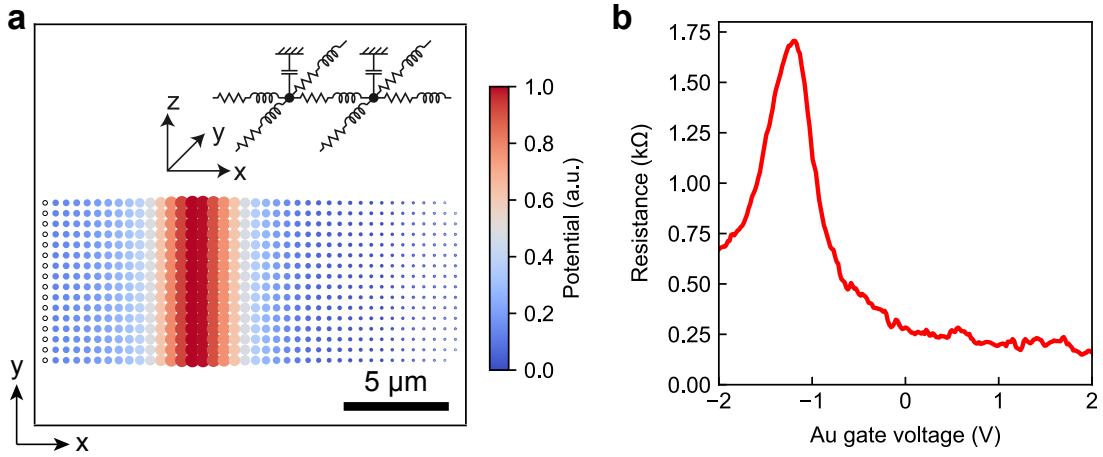


Figure S4 | Waveform simulation of acoustic plasmon wavepackets. **a**, Snapshot of plasmon transport at a carrier density of $n = 10.6 \times 10^{11} \text{ cm}^{-2}$ and time delay of 2.0 ps. The size and color of each dot indicate the potential at individual nodes in the distributed constant circuit. The inset illustrates the elements, R , L , and C , constituting each node. The spacing between nodes is $0.5 \mu\text{m}$. Plasmons are injected from the leftmost points, indicated by black open circles. Here, the echo pulse is excluded for clarity. **b**, DC resistance of graphene plotted as a function of the Au gate voltage.

PC switches. The echo pulse is calculated by multiplying the amplitude of the initial pulse by the reflection factors r_g and r_d , and adding the time delays τ_g and τ_d . Here, the subscripts g and d represent the generation and detection PC switches, respectively. We used $\tau_g = 6.14$ ps and $\tau_d = 5.78$ ps obtained from the known distance between the graphene and the two PC switches, along with the known v_{CPW} . For the reflection factors, we employed $r_g = r_d = 0.2$. The simulation results, plotted in Fig. 4a of the main text, show good agreement with the experimental waveform.

The crossover between coherent plasmon transport and incoherent diffusive transport occurs at $k^2/LC \sim R^2/4L^2$. Eq. (S2) gives plasmon transport for $k^2/LC \gg R^2/4L^2$ and diffusive transport for $k^2/LC < R^2/4L^2$. In the diffusive transport regime, the peak of a solitary pulse remains at the injection sites. The temporal maximum of a diffusive wave at distance x appears when $t = RC^2x^2/2$, and the velocity of this peak is slower than the plasmon velocity by a factor of $3/(R/2\sqrt{C/L}x)$.

IV. Conductive and capacitive coupling to an acoustic plasmon

As shown in Fig. S5, the coupling strength between acoustic plasmons in graphene and the electrical pulse in the CPW can be controlled by tuning V_{ZnO} . At high carrier density

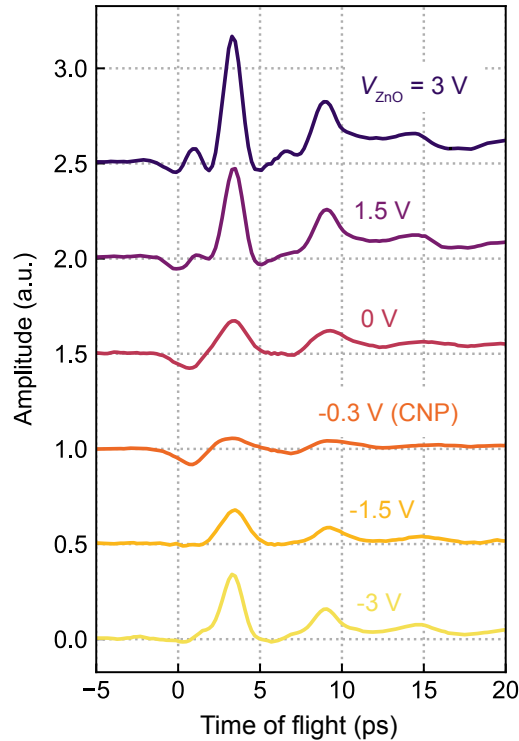


Figure S5 | Coupling control to an acoustic plasmon. Time domain waveforms of acoustic plasmons ($V_{Au} = 1.5$ V) in the Au gate device for different values of V_{ZnO} .

($|V_{\text{ZnO}}| = 3 \text{ V}$), the waveform takes on a cosinusoidal shape, indicating conductive coupling between graphene and the CPW due to small resistance. Conversely, near the CNP ($V_{\text{ZnO}} = -0.3 \text{ V}$), the waveform becomes sinusoidal, suggesting capacitive coupling due to large resistance. All measurements presented in the main text were performed at $V_{\text{ZnO}} = 3 \text{ V}$.

References

1. Wu, J. *et al.* Excitation, detection and electrostatic manipulation of terahertz-frequency range plasmons in a two-dimensional electron system. *Sci. Rep.* **5**, 15420 (2015).
2. Das Sarma, S. & Hwang, E. H. Collective modes of the massless Dirac plasma. *Phys. Rev. Lett.* **102**, 1–4 (2009).
3. Nikitin, A. Y., Guinea, F., García-Vidal, F. J. & Martín-Moreno, L. Edge and waveguide terahertz surface plasmon modes in graphene microribbons. *Phys. Rev. B* **84**, 161407 (2011).
4. Sasaki, K. & Kumada, N. Effects of screening on the propagation of graphene surface plasmons. *Phys. Rev. B* **90**, 035449 (2014).
5. Kumada, N. *et al.* Plasmon transport and its guiding in graphene. *New J. Phys.* **16**, 063055 (2014).